URANS simulation of injection-driven flows with an imposed-transition model

B. Gazanion, F. Chedevergne, G. Casalis

URANS Simulation of Injection-Driven Flows with an Imposed-Transition Model

B. Gazanion[1,2], F. Chedevergne [*2], and G. Casalis[2]

[1]CNES, 52 Rue Jacques Hillairet, 75612 Paris CEDEX, FRANCE
[2]ONERA, 2 Avenue Edouard Belin, 31055 Toulouse CEDEX, FRANCE

Abstract

The influence of laminar-turbulent transition on injection-driven flows fluctuations is investigated. URANS simulations of the transitional flow are compared with a laminar simulation and a cold-flow experiment. The transition in the URANS simulations is imposed using an intermittency function based on experimental observations by Gazanion *et al.* [13]. The simulations evidence a strong influence of the transition on the flow fluctuations. In particular, the amplification of PVS modes is reduced in the transition region, and the vortical structures are damped. The influence of the parameters of the transition model in these phenomena is detailed. It is also showed that using the transition model can improve the relevance with the experiment.

1 Introduction

A long and segmented Solid Rocket Motor (SRM) may exhibit thrust oscillations during its firing. This phenomenon of prior importance results from instabilities of the SRM flow.

The own flow of the gaseous combustion products in the chamber holds vortex shedding phenomena. The associated instability may originate from geometric features of the chamber, such as inhibitors or cavities. Besides, the flow induced by injection at the duct walls, the so-called injection-driven flow which represents the flow in a SRM, is fundamentally unstable. There is indeed a powerful intrinsic instability, named Parietal Vortex Shedding (PVS). Due to the PVS modes, coherent vortical structures are simultaneously convected by the mean flow and spatially amplified. Upon reaching the nozzle critical section, a backward pressure wave is generated. When the corresponding frequencies couple with the ones of the pipe acoustics modes, pressure oscillations arise which finally induce the thrust oscillations.

[*]Francois.Chedevergne@onera.fr

Cold flow experiments, reproducing the injection-driven flow, support the existence of this coupling, even in a pure cylinder geometry. Recent theoretical developments [6, 8, 4] have lead to a relevant stability method for laminar injection-driven flows which accurately predicts the oscillation frequencies.

A laminar-turbulent transition is likely to occur when the duct aspect ratio, *i.e.* the ratio of length over radius, is large. The turbulent structures may interact with the coherent vortices induced by PVS. Damping is likely to occur and consequently reduce the inner pressure oscillations. Turbulence in injection-driven flows is still poorly understood. Most studies using URANS approaches focused on planar configurations, such as that of Traineau *et al.* [18] or Avalon *et al.* [2], and on the turbulence model [16, 3]. URANS simulations show that pressure oscillations can be reduced when the flow is turbulent, depending on the turbulence level [12]. However most of the time the laminar-turbulent transition is neglected, which can lead to severe discrepancies on the turbulence properties [9]. The computations are usually either fully laminar or fully turbulent (URANS).

The present work consists in a numerical study of the influence of the laminar-turbulent transition on the pressure oscillations in a cylindrical geometry. URANS simulations are performed for an axisymmetric geometry, and the transition is imposed using an intermittency function. Comparisons with a reference laminar simulation and measurements assess the effect of transition. Furthermore, the influence of the transition model parameters is studied.

2 Experimental investigation of laminar-turbulent transition

A brief summary of the analysis of experimental measurements presented by Gazanion *et al.* [13] is firstly given in the present paper. Their analysis focused on instantaneous velocity properties in order

to build a local description of the laminar-turbulent transition, which will be implemented in the numerical simulations presented thereafter.

2.1 Cold-flow setup VALDO

VALDO is a cold-flow setup reproducing the injection-driven flow in a cylindrical duct. It was operated at ONERA by G. Avalon and D. Lambert from 2000 to 2011 [1]. The setup principle is that of Yagodkin[19] and Brown *et al.* [5], namely a porous-walled duct enclosed in a pressurized chamber. The pressure difference between the chamber and the vein creates a uniform gas injection through the duct.

The setup configuration is shown on fig. 1. It is made of four independent elements assembled together, each one mainly composed by a porous cylinder and its feeding chamber. The resulting vein is a cylinder of radius $R = 30\,\text{mm}$ and length $L = 672\,\text{mm}$. One section named head-end is closed, and the other one is an open exit. The duct porosity is $18\,\mu\text{m}$ and the feeding pressure P_f is $3.5\ 10^5\,\text{Pa}$, leading to an injection velocity $V_{inj} = 1.05\,\text{m.s}^{-1}$.

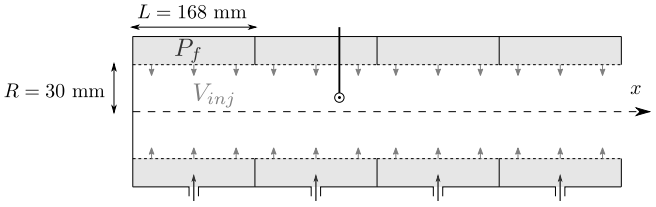

Figure 1: Geometry of the VALDO setup

Velocity measurements are performed with a single-wire constant temperature anemometer. The probe is inserted in the vein through a dedicated injection element. Permutations of the elements enabled measurements at 8 different axial positions. For a given axial position, measurements were performed at 30 positions over the diameter. The streamwise instantaneous velocity U, *i.e.* the norm of the velocity normal to the probe wire $||(V_r, 0, V_z)||$, and the pressure are sampled during 1 s at 4000 Hz.

2.2 Velocity signal analysis

For injection-driven flows, the laminar and turbulent profiles of mean velocity are quite close, contrary to the laminar and turbulent boundary layer profiles. Besides, the velocity signals do not exhibit clear transitional features such as intermittency spots. A specific analysis was therefore proposed in order to distinguish the laminar and turbulent states, and to highlight the transition. The focus was set on the frequential content of the velocity signals.

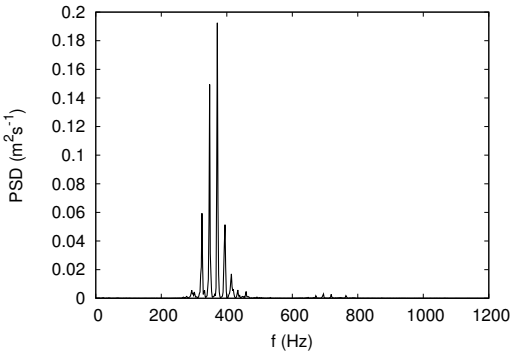

Figure 2: PSD of a laminar velocity signal

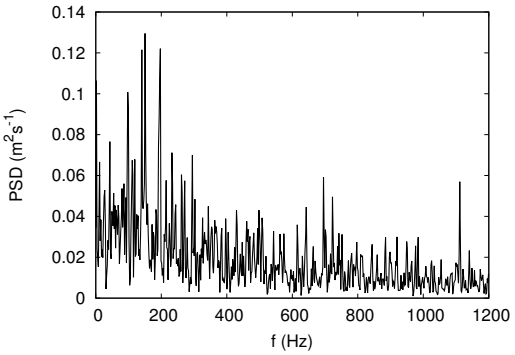

Figure 3: PSD of a turbulent velocity signal

The Power Spectral Density (PSD) of the velocity signal for the laminar state (fig. 2) exhibits a few number of discrete modes. This pattern, with the corresponding frequencies, is characteristic of the Parietal Vortex Shedding (PVS) theoretically predicted by biglobal analysis of the mean laminar flow [8, 4]. Consequently this figure illustrates the frequential signature of the laminar state.

The PVS is an injection-driven flow intrinsic instability characterized by a finite number of discrete modes. The modes are temporally damped and spatially amplified in the axial direction. The frequencies of the excited modes, visible on fig. 2, are close to the first longitudinal acoustic (pipe) mode.

On the contrary, the PSD of the turbulent signal (fig. 3) is devoid of leading frequencies. A comparison of these figures shows that PSD enables a simple distinction of the laminar and turbulent state.

More generally, processing methods sensitive to the unsteady properties of the signal seem adequate for the present analysis. Autocorrelation and statistics of the velocity signal were proven relevant and included in the analysis. A numeric factor $\mathcal{C}$ describing the local level of turbulence was built upon those methods. Contours of $\mathcal{C}$ are drawn on fig. 4

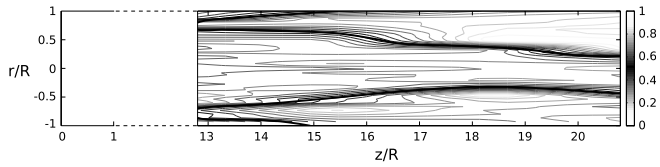

Figure 4: Contours of $\mathcal{C}$

The black smooth line indicates the location of laminar-turbulent transition according to the criterion $\mathcal{C} = 0.5$ chosen by Gazanion *et al.* [13]. It separates a core of laminar flow from lateral regions of turbulent flow.

The coexistence of laminar and turbulent regions downstream of $z/R = 12$, see fig. 4, supports the necessity for a transition model in numerical simulations. The model aims at reproducing the laminar-turbulent transition highlighted in the experiment, using the same shape for the transition region.

3 Numerical procedure

3.1 The CEDRE code

Numerical simulations are conducted with the CEDRE solver developed at ONERA [15]. The CEDRE code is a simulation platform for multi-physics applications in energetics. The platform couples solvers dedicated to specific features of these fields, such as multi-phase flows, radiation, conduction, thin films and reactive flows. To address the complexity of applications, the CEDRE code is massively parallel and manipulates unstructured meshes.

The CEDRE code is widely used for the simulation of SRM mechanisms, such as base flow instability [8, 4], multiphase physics [17, 10] and thermoacoustic instabilities [7].

The present simulations rely on the compressible solver CHARME of the CEDRE code. Reynolds-Averaged Navier-Stokes equations are solved using a second-order finite-volume formulation. Time integration uses a second-order explicit Runge-Kutta scheme for unsteady simulations. A first-order implicit Euler method ensures the convergence for steady simulations.

3.2 Imposed laminar-turbulent transition method

The laminar-turbulent transition method consists in a limitation of the eddy viscosity predicted by the RANS model :

$$\mu_t = \gamma \, \mu_t^{RANS} \tag{1}$$

The limiter γ can be considered as a numerical intermittency function. It is null in laminar flow regions and equal to 1 in turbulent flow regions. The spatial evolution of γ, which determines the transition properties, is an input of the present simulations.

The transition model is intended to cancel the dissipation of velocity fluctuations, due to turbulence, in the laminar region. Turbulent dissipation indeed prevents the creation of PVS vortices, by damping the perturbations in the flow.

The intermittency function for the simulation is built upon a reference contour of transition development, noted $\mathcal{L}$. By definition, the points of this line have the same level of transition development, which is represented by an intermittency function value γ_0. It is assumed that the transition region spread over a finite width D along the local normal to $\mathcal{L}$. Therefore, the intermittency function γ can be defined upon the algebraic distance to $\mathcal{L}$.

$$\gamma = f(d, D, \gamma_0)$$

In this expression, d is the algebraic distance to the reference line $\mathcal{L}$, D is the width of the transition region and γ_0 is intermittency function value associated to $\mathcal{L}$. To avoid a steep transition, f follows a hyperbolic tangent law mainly based on the algebraic distance. The role of D and γ_0 is illustrated below in fig. 5.

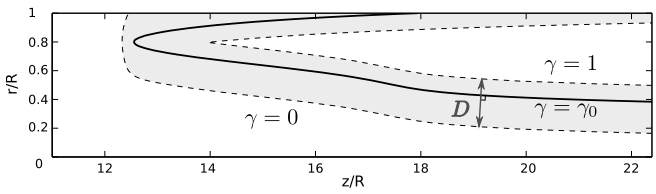

Figure 5: Transition region

A simplified shape of $\mathcal{L}$ is deduced from the experimental work of Gazanion *et al.* [13]. It is represented by a plain line in fig. 5. However the parameters γ_0 and D are not easily deduced from the experiments. Arbitrary values are chosen. The influence of these values will be discussed in section 4.3.

The contours of γ are represented in fig. 6 in the axisymmetric computational domain, with exact scale ratio. This example was computed with the experiment-based simplified shape, a width $D = R/3$ and an intermittency function value $\gamma_0 = 0.9$.

Instead of a limitation of the production terms in the turbulent scalar equations, the transition model is a direct limitation of the eddy-viscosity. This is not critical since the injection-driven flow studied

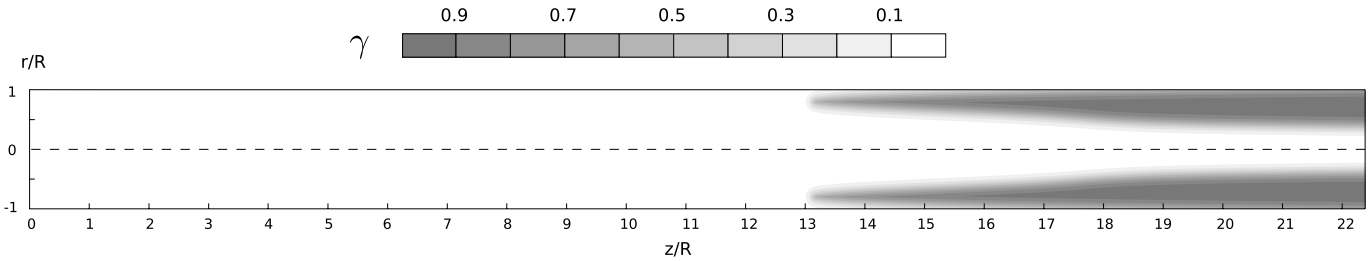

Figure 6: Isovalues of γ, computed with the experiment-based reference line, $D = R$ and $\gamma_0 = 0.5$

in this work is strongly convective. Indeed the injection rate V_{inj}/u_τ[1] is high since it is superior to 5 on the whole length of the injecting wall. As a consequence, the turbulent scalars have weak production and dissipation, and stay close to their injection values. The precise injected values of the turbulent scalars are not important, provided that the resulting turbulent viscosity is relevant in the turbulent region. The production term of the turbulent kinetic energy, k, has a turbulent viscosity at the denominator. It was replaced by μ_t^{RANS}, *i.e.* the turbulent viscosity without limitation, to prevent abnormal productions when the flow is set laminar and the intermittency function is null.

3.3 Simulation parameters

The inner geometry of the experimental setup (VALDO) is represented as a bi-dimensional axisymmetric domain of length $L = 672\,\text{mm}$ and radius $R = 30\,\text{mm}$. The domain boundaries are the symmetry axis at $r = 0$, an injecting wall at $r = R$, an impermeable wall at $z = 0$ and a free exit at $z = L$. The fluid is air close to atmospheric pressure and 300 K.

The injecting wall is treated as a velocity inlet $V_{inj} = 1\,\text{m.s}^{-1}$ on the radial direction, with imposed values for the turbulent scalars. A slip condition is used for the head-end impermeable wall ($z = 0$), and the exit is a subsonic velocity outlet at the mean pressure $1.013\ 10^5$ Pa. A $N_z \times N_r = 1000 \times 150$ structured grid is used. A slight refinement is performed near the head-end over a few percent of the length, while the grid is uniform in the radial direction.

The simulation procedure is split in two steps. First, a steady flow is computed using a uniform injection and a first-order implicit time integration, with a large time step. Then, a spatial perturbation is added to the injection condition and an unsteady simulation is proceeded with a second-order explicit temporal scheme, using the steady flow as an initial condition. The spatial perturbation consisting in a local interruption of the velocity inlet over two cells is commonly used, see *e.g.* [7], in order to excite the PVS (which is temporally stable, as recalled before). The time-step for this simulation is $2\ 10^{-}7\,\text{s}$, leading to a CFL number of 0.4.

The turbulence model used for the transitional simulations is the $k - \omega$ BSL of Menter[14]. The values of the turbulent scalars imposed at the injecting wall are noted k_w and ω_w. k_w is a pseudo-turbulence [3], estimated with the average velocity fluctuations measured experimentally on the wall surface. The fluctuations magnitude is 10% V_{inj}, which leads to $k_w = 5\ 10^{-3}\,\text{m}^2.\text{s}^{-2}$. ω_w is estimated from :

$$\omega_w = C_\mu^{-1/4}\ \frac{\sqrt{k_w}}{l_w}\ , \qquad \text{with } C_\mu = 0.09 \qquad (2)$$

with l_w taken as $R/5$, an asymptotic value corresponding to the turbulent pipe flow theoretically reached far downstream of the computation domain.

4 Results

4.1 Foreword

The ONERA in-house CEDRE code solves the Navier-Stokes equations for compressible gas, so there are intrinsically acoustic modes in the simulations. On the contrary, the experimental setup is almost devoid of acoustics because of its open exit. This leads to a difference between simulations and experiments.

The hydrodynamic fluctuations (PVS) induce a vorticity component but very low pressure fluctuations. Consequently, the measured pressure fluctuations are mainly due to acoustic modes and will be assimilated to acoustics in the following. Besides, considering the geometry, the acoustic modes consist in planar waves (pipe flow). Their contribution to the radial velocity fluctuations is null, and even negligible if the *vorticity correction* is taken into account, see [11].

[1] u_τ is the friction velocity, computed near the injecting wall for the theoretical Taylor-Culick mean flow

As a summary, the temporal fluctuations of the flow variables can be theoretically related to different combinations of phenomena. The pressure p measures acoustics effects, the radial velocity component v_r results from PVS effects, and the axial velocity component v_z is a consequence of both acoustics and PVS effects. Subsequently, PVS-related aspects are investigated considering v_r.

The unsteady simulations begin with a transient state during which the pressure oscillations and the PVS modes grow in the domain. This state ends when a quasi-periodic flow with converged statistical properties is established. The fluctuations are computed on the converged state, from $t_i = 0.15\,\mathrm{s}$ to $0.3\,\mathrm{s}$.

4.2 *Influence of laminar-turbulent transition*

We now investigate the results obtained when the transition is taken into account by a comparison to a fully laminar simulation. The fluctuations of radial velocity are compared at the radial position where they are the higher, namely $r/R = 0.8$.

Axial profiles of the root-mean-square (RMS) pressure fluctuations, see fig. 7, highlight a clear acoustic phenomenon in both simulations. This acoustics is linked with the boundary condition chosen for the exit. The presence of a pressure node at the exit ($z/R \approx 672\,\mathrm{mm}$) shows that this boundary condition is reflective. The dominant acoustic mode is the same in the two simulations, however the pressure fluctuation amplitudes are significantly reduced when the transition is taken into account.

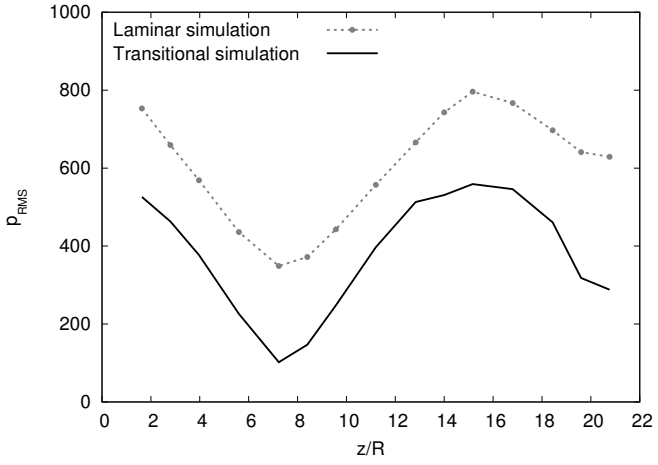

Figure 7: Axial evolution of near-wall ($r/R = 0.8$) RMS pressure fluctuations

A comparison of the vorticity fields is presented in fig. 8. The upper part *(a)*, corresponding to the laminar simulation, is firstly examined. For low values of z/R and close to the injecting wall, the horizontal strips of the acoustic boundary layer are visible. A spatial perturbation is introduced at $z/R = 5.6$, as explained earlier. The emergence of PVS modes and their spatial amplification is evidenced downstream. The high rotational lines inclined in the opposite direction to the flow are characteristic of PVS vortical structures. A more complex behaviour arises downstream of $z/R = 15$.

The vorticity field of the transitional simulation, *(b)*, is similar to that of the laminar simulation up to $z/R = 12$. It indeed shows the acoustic boundary layer and the amplification due to PVS. Meanwhile discrepancies arise from the beginning of the transition region, at $z/R \approx 13$ for $r/R \approx 0.8$. The comparison of the fields of fig. 8 highlights a vorticity damping downstream of the transition beginning.

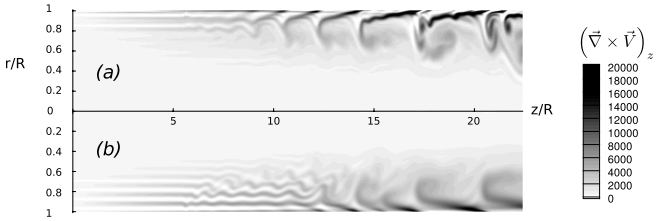

Figure 8: Field of vorticity for *(a)* the laminar simulation and *(b)* the transitional simulation

At last, the focus is set on the amplification of PVS modes. As explained earlier, the comparison is based on the RMS values of v_r. The axial evolution close to the injection wall is represented on fig. 9.

For small values of z/R, the amplitudes in both simulations are small, only acoustics fluctuations exist close to the head-end as depicted by figure 6. Then there is a clear amplification which comes from the spatial growth of the PVS. The slope (*i.e.* the amplification) is very similar between the two simulations. However it must be noted that the growth starts earlier in the simulation with the transition included. On the other hand, the amplification remains nearly constant in the laminar simulation whereas it is strongly reduced when the transition is taken into account. The PVS growth is strongly affected by the transition, as expected.

The comparison of a laminar simulation and a transitional simulation, *i.e.* using the imposed transition method, has highlighted a significant influence of the transition on the unsteady flow. First of all, the transition leads to a reduction of the fluctuation levels in the flow. This reduction concerns the pressure fluctuations (fig. 7), and the vorticity intensity (fig. 8). The PVS amplification seems to start earlier when transition is included, see fig. 9. The amplification itself is not influenced up to the transition onset, whereas transition induces down-

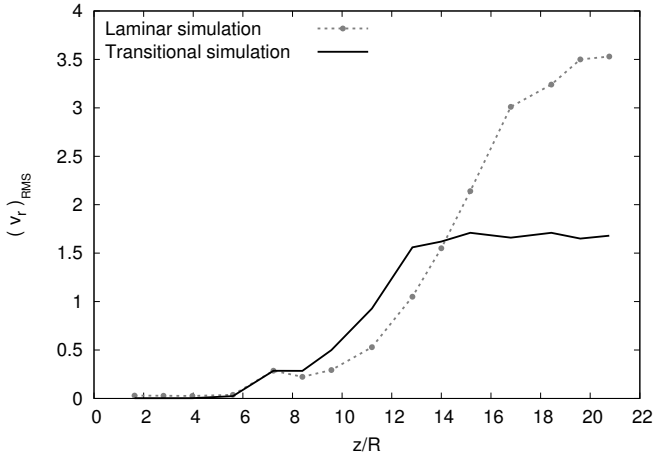

Figure 9: Axial evolution radial velocity fluctuations close to the injecting wall ($r/R = 0.8$)

stream a strong reduction of the amplification.

4.3 *Influence of transition parameters*

The imposed transition method presented in this paper uses an intermittency function describing the transition region which is modelled by three parameters: the reference line, the width D and the intermittency function value γ_0 attributed to the reference line. The reference line $\mathcal{L}$ gives the general shape of the transition region, and the other parameters its width and position. The sensitivity of the transition method on each parameter of the intermittency function is now investigated.

4.3.1 Reference line: First of all the focus is set on the line $\mathcal{L}$ toward which the algebraic distance is defined. According to the computation of γ and the related hypothesis, this parameter gives the shape of the transition region in the simulations.

Three sets of parameters for γ are considered to highlight the influence of the reference line. For set S_1, the reference line is the simplified shape extracted from the experiment and represented on fig. 5. The two other sets of parameters use a vertical reference line ; it is located at $z_0/R = 12$ for S_2 and at $z_0/R = 15$ for S_3. For the three sets, the transition region width is $D = R$ and the intermittency function value on the reference line is $\gamma_0 = 0.5$.

The comparison is based on the evolution of the radial velocity fluctuations, $(v_r)_{RMS}$, see fig. 10. The radial component of velocity is a good indicator of PVS amplification, as explained above.

The three simulations exhibit a common behaviour. First, a relatively small perturbation appears at the first position after the injection break. It is followed by a growth step revealing of the PVS modes amplification. At last, a slope breakdown occurs in the transition region. More precisely, it seems to occur when $\gamma \approx 0.5$, which is easily visible when $\mathcal{L}$ is vertical.

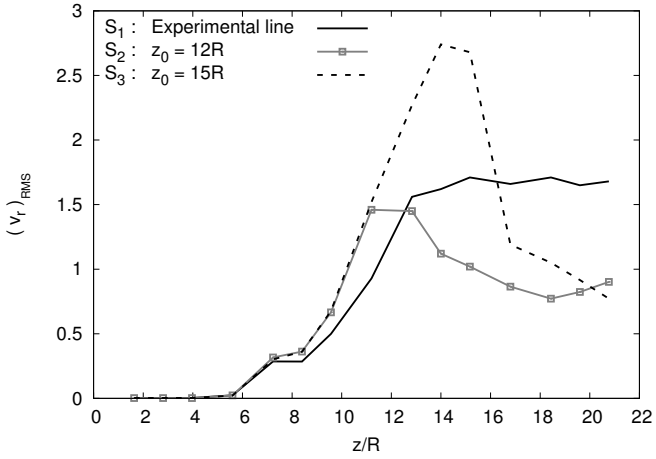

Figure 10: RMS of radial velocity fluctuations close to the injecting wall ($r/R = 0.8$)

The growth rate is significantly modified by the shape of the transition region, *i.e.* that of $\mathcal{L}$, even far before transition takes place. This shows that the transition has an influence on velocity fluctuations in the whole domain.

The delayed transition with S_3, compared to the transition with S_2, leads to a stronger level for PVS modes before the transition. As a consequence the fluctuation amplitude decrease after the transition start is much sharper. The transition with S_1 seems smoother since it only counterbalances the PVS amplification.

4.3.2 Influence of the transition width D: For this comparison, γ is computed with the reference line based on the experiment and $\gamma_0 = 0.5$. Three values of the transition region width D are considered, namely R/3, R and 5R/3.

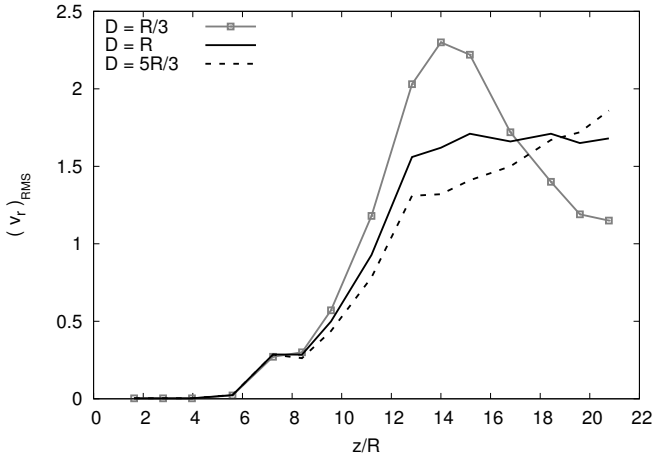

Figure 11: RMS of radial velocity fluctuations close to the injecting wall ($r/R = 0.8$)

First of all, fig. 11 confirms that the slope break-

down occurs when $\gamma \approx 0.5$. In this case it is located at z/R between 12.8 and 14.

Three behaviors arise within the range of transition region width D considered. After the slope breakdown, $(v_r)_{RMS}$ decreases for $D = R/3$, stagnates for $D = R$, and increases at a lower rate for $D = 5R/3$. Furthermore, the growth rate before the transition is also affected by D. Indeed a steeper transition, *i.e.* a lower D, leads to a stronger growth rate.

4.3.3 *Influence of the intermittency function value γ_0 on the transition line:*

For this study the width of the transition region is set to $D = R$, and the reference line is the experiment-based one.

Because $\mathcal{L}$ is convex and D is large, changing γ_0 results in more than a simple shift of the transition region. In particular, the axial width of the transition region and the position where $\gamma \approx 0.5$ is reached are strongly modified. The profiles for three values of γ_0, see fig. 12, indeed exhibit significant differences.

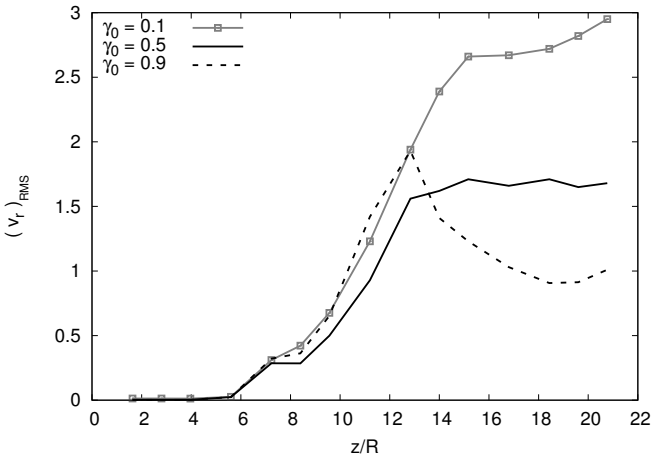

Figure 12: RMS of radial velocity fluctuations close to the injecting wall ($r/R = 0.8$)

First of all, as a consequence of the reference line convexity and aspect ratio, the position of the slope breakdown is quite close for $\gamma_0 = 0.5$ and $\gamma_0 = 0.9$ but strongly delayed for $\gamma_0 = 0.1$.

For $\gamma_0 = 0.9$, the transition at $r/R = 0.8$ is very steep in the axial direction. Therefore the profile undergoes a strong decrease as soon as the transition starts. On the contrary for $\gamma_0 = 0.1$ the large transition region leads to a slower increase after the slope breakdown. This pattern is quite similar to that observed in fig. 11 for $D = 5R/3$, with a higher fluctuation level coming from the delayed transition.

A modification of the amplification rate before the transition is also observed. It is much probably a consequence of the difference of transition width in the axial direction, resulting from the difference of γ_0 as mentioned earlier.

4.3.4 *Summary:*

A parametric study of the three parameters used for the transition model has been presented. In all these cases, the global effect of the transition model on the flow is the same as observed in section 4.2, namely a damping of PVS fluctuations. The three parameters all have a significant influence on the radial velocity profile. The main differences were on the position of the slope breakdown and the profile behaviour downstream. A common feature is their influence on the levels of $(v_r)_{RMS}$. It was also evidenced that the parameters of the transition have an impact on the velocity profile even far upstream of the transition region.

A key element in the effect of the transition region seems to be its steepness in the axial direction. For both parameters involved and in the ranges considered, it has been observed that the steeper the transition is, the more the velocity fluctuations are damped.

Another important element is the level of PVS amplification reached before the turbulent viscosity becomes significant. Indeed the most severe differences on the velocity amplitudes are observed when the parameters affect the position of the transition centerline.

4.4 *Comparison with experiments*

The simulations are now compared with measurements from the cold-flow experiment VALDO, presented earlier. The experimental measurement essentially consist in local velocity measurements. A comparison with the simulation requires to find a physical quantity with the same signification in both approaches.

The hot-wire probe measures the velocity normal to its wire. In the considered measurements, the wire is normal to both the radial and axial directions, so the azimuthal component of the velocity is not captured. The instantaneous measured velocity is therefore $||(V_r, 0, V_z)||$, where $||.||$ is the L_2 norm.

An equivalent velocity is computed for the simulation from V_r and V_z. It is defined as :

$$U = ||(V_r, 0, V_z)|| \tag{3}$$

This velocity, named streamwise velocity, has the same signification in the simulations and in the experiment. In both situations, its fluctuating part is computed as :

$$u = U - \overline{U} \tag{4}$$

The comparison is led upon the amplitude of streamwise velocity fluctuations, represented by

$u_{RMS} = \sqrt{\overline{u^2}}$. The profiles for the experiment, the laminar simulation and a transitional simulation are shown in fig. 13. For the transitional simulation, the intermittency function in the transition region is computed toward the experiment-based reference line, with $D = R$ and $\gamma_0 = 0.5$.

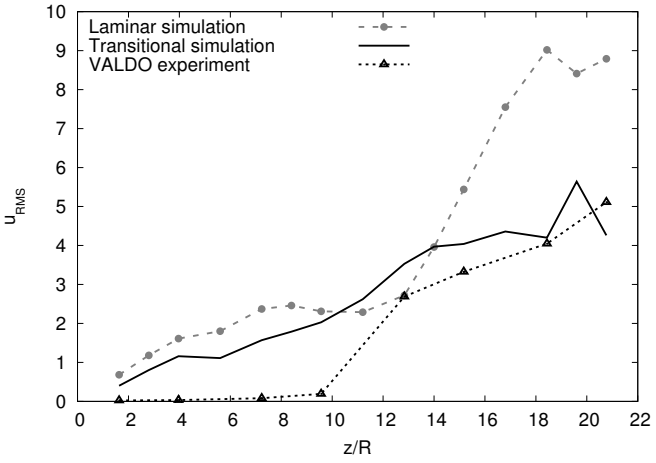

Figure 13: Streamwise velocity fluctuations close to the injecting wall ($r/R = 0.93$)

The streamwise velocity includes the axial velocity, so it is affected by potential acoustics fluctuations. The influence of acoustics is most likely responsible for the gap between the profiles at $z/R < 9$. As mentioned earlier, the experiment is nearly devoid of acoustics.

The presence of acoustics in the simulations complicates the comparison with the experiment. For instance, the amplification rate based on the streamwise velocity can be affected in the simulations. Indeed the transitional simulation and the laminar simulation exhibit different growths for u, while it was previously showed with v_r, see fig. 9, that the amplification of PVS modes was the same.

Differences between the two simulations for low values of z/R are probably due to the transition, whose influence on fluctuations in the whole domain has been highlighted. Downstream the transition start, the fluctuation amplitude in the transitional simulation is close to the experimental fluctuation values, while it is much higher for the laminar simulation. In this region the influence of acoustics is less important. In that sense, fig. 13 shows that using the transition model improves the agreement of the simulations with the experiment.

5 Conclusion

The injection-driven flow in a cylindrical duct was simulated by a URANS approach. An imposed transition method was implemented to account for the laminar-turbulent transition of this flow. This method uses an intermittency function to describe the transition region properties. In particular, a calculation of intermittency function representative of the transition in a reference experiment was derived.

Simulations with the transition method were compared to a reference laminar simulation. A damping of fluctuations as well as a strong reduction of axial amplification were observed. Those effects of the laminar-turbulent transition were expected, however to the authors knowledge it had still not been explicitly demonstrated.

The influence of the intermittency function parameters on the flow features were investigated. The transition method proved to be relevant for the range of parameters tested. Finally, the streamwise velocity amplification was compared between the simulations and the experiment. The transitional simulation is more representative of the experiment than the laminar simulation.

This work proved that taking account of the transition into RANS simulations significantly modified the prediction of the oscillatory behaviour of the flow. The Reynolds-averaged simulation of an injection-driven flow is still a complex problem. In particular, the choice of the turbulence model and the related injected scalars remains an opened question.

Acknowledgement

This work was supported by the french space agency CNES and by ONERA.

References

[1] G. Avalon and T. Josset. Cold gas experiments applied to the understanding of aeroacoustic phenomena inside solid propellant boosters. AIAA, July 2006.

[2] G. Avalon, B. Ugurtas, F. Grisch, and A. Bresson. Numerical computations and visualization tests of the flow inside a cold gas simulation with characterization of a parietal vortex shedding. Huntsville, July 2000. AIAA.

[3] R. A. Beddini. Injection-induced flows in porous-walled ducts. *AIAA Journal*, 24(11):1766–1773, 1986.

[4] G. Boyer, G. Casalis, and J.-L. Estivalèzes. Stability and sensitivity analysis in a simplified solid rocket motor flow. *Journal of Fluid Mechanics*, 722:618–644, 2013.

[5] R. S. Brown, R. Dunlap, S. W. Young, and R. C. Waugh. Vortex shedding as a source

of acoustic energy in segmented solid rockets. *Journal of Spacecraft and Rockets*, 18:312–319, July 1981.

[6] G. Casalis, G. Avalon, and J.-P. Pineau. Spatial instability of planar channel flow with fluid injection through porous walls. *Physics of Fluids*, 10:2558, 1998.

[7] G. Casalis, G. Boyer, and E. Radenac. Some recent advances in the instabilities occurring in long solid rocket motors. In *47th AIAA/ASME/SAE/ASEE Joint Propulsion Conference and Exhibit*. American Institute of Aeronautics and Astronautics, 2011.

[8] F. Chedevergne, G. Casalis, and J. Majdalani. Direct numerical simulation and biglobal stability investigations of the gaseous motion in solid rocket motors. *Journal of Fluid Mechanics*, 706:190–218, 2012.

[9] A. Ciucci, G. Iaccarino, R. Moser, F. Najjar, and P. Durbin. Simulation of rocket motor internal flows with turbulent mass injection. *Proc. Summer Prog. Center for Turbulence Research, Stanford University*, page 245–266, 1998.

[10] F. Doisneau, A. Sibra, J. Dupays, A Murrone, F. Laurent, and M. Massot. Numerical strategy for unsteady two-way coupled polydisperse sprays: Application to solid-rocket instabilities. *Journal of Propulsion and Power*. To appear.

[11] G. A. Flandro and J. Majdalani. Aeroacoustic instability in rockets. *AIAA Journal*, 41(3):485–497, March 2003.

[12] S. Gallier, F. Godfroy, and F. Plourde. Computational study of turbulence in a subscale solid rocket motor. In *40th AIAA/ASME/SAE/ASEE Joint Propulsion Conference and Exhibit*. American Institute of Aeronautics and Astronautics, 2004.

[13] B. Gazanion, F. Chedevergne, and G. Casalis. On the laminar-turbulent transition in injection-driven porous chambers. *Experiments in Fluids*, 55(1):1–13, January 2014.

[14] F. R. Menter. Improved two-equation k-omega turbulence models for aerodynamic flows. Technical Report 103975, NASA, Ames Research Center, 1992.

[15] A. Refloch, B. Courbet, A. Murrone, P. Villedieu, C. Laurent, P. Gilbank, J. Troyes, L. Tessé, G. Chaineray, J.-B. Dargaud, et al. CEDRE software. *Aerospace Lab*, 2:1–10, 2011.

[16] J. Sabnis, R. Madabhushi, H. Gibeling, and H. McDonald. On the use of the k-e turbulence model for computation of solid socket internal flows. Monterey, 1989. AIAA.

[17] A. Sibra, J. Dupays, F. Laurent, and M. Massot. A new eulerian multi-fluid model for bi-component polydisperse sprays: an essential approach to evaluate the impact of aluminum combustion on solid rocket motor instabilities. American Institute of Aeronautics and Astronautics, July 2013.

[18] J.-C. Traineau, P. Hervat, and P. Kuentzmann. Cold-flow simulation of a two-dimensional nozzleless solid rocket motor. *Rep./AIAA*, 1986.

[19] V. I. Yagodkin. Use of channels with porous walls for studying flows which occur during combustion of solid propellants. In *Proceedings of the 18 th International Astronautical Congress*, volume 3, pages 67–79, 1967.